RESEARCH ARTICLE SUMMARY

NANOPARTICLE ASSEMBLY

Decoding collective dynamics and complexity in nanoparticle assemblies using graph theory

Jonas Hallstrom†, Puquan Pan†, Jayson Sia† *et al.*

Full article and list of author affiliations: https://doi.org/10.1126/science.aeb5134

INTRODUCTION: Nanoparticles (NPs) occupy a unique intermediate scale between molecules and colloids, exhibiting self-assembly behaviors that combine characteristics of both but remain fundamentally distinct, often resulting in complex structures that combine order and disorder. These partially organized states, including chains, clusters, pores, and low-density networks, are critical for technological applications yet remain challenging to quantify using traditional symmetry-based descriptors. A general methodology to quantitatively describe these low-order, low-density states is essential for advancing applications that exploit their optical, mechanical, and electrical properties.

RATIONALE: We provide graph theory (GT) as a mathematical framework to characterize dynamic NP systems transitioning from dispersions of free particles to fully assembled colloidal crystals. Using wide-frame time-resolved liquid-phase transmission electron microscopy (LPTEM), we tracked >400 gold nanocubes in real time, supplemented by molecular dynamics (MD) and kinetic Monte Carlo (kMC) simulations of systems containing up to 10,000 particles. We focused on two new GT metrics: Ollivier-Ricci curvature (ORC), which captures global structural and transport patterns by quantifying how local interactions propagate through neighborhoods beyond nearest neighbors, and augmented Forman-Ricci curvature (AFRC), which quantifies local robustness through three-particle cluster dynamics. ORC provides a continuous measure of structural complexity, with negative values indicating bridging edges between communities and near-zero values representing regular lattices. AFRC tracks the formation and dissolution of energetically unfavorable three-particle cycles, serving as a proxy for system energy and reconfigurability.

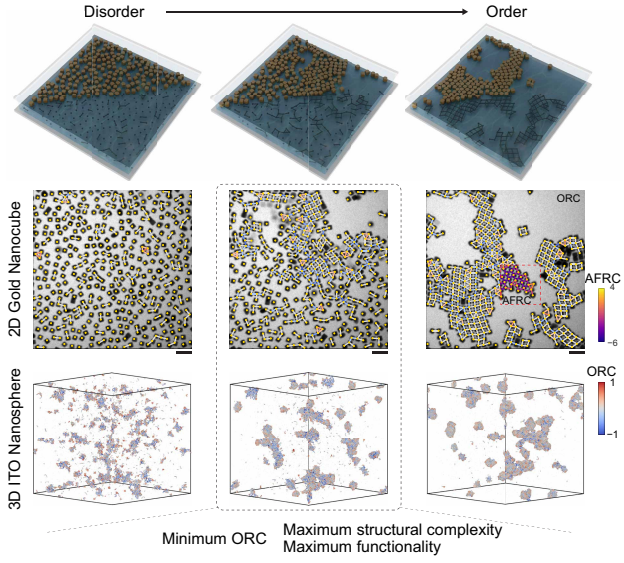

Graph curvature measures quantify disorder and complexity for self-assembled particle systems. NP assemblies can be viewed as a series of graphs or networks in which nodes represent NPs and edges represent strong interparticle interactions. ORC and AFRC can be found for every edge in these graphs, quantifying the structural order and complexity in the local area around those edges. Scale bars, 200 nm.

RESULTS: Analysis of gold nanocube assembly revealed three distinct stages characterized by ORC trajectories. Both the initial and final stages of the assembly showed near zero average ORC due to their near perfect disorder and order, respectively, whereas the intermediate stage exhibited strongly negative ORC, corresponding to the formation of dynamic mesocrystals (groups of 4 to 20 aligned NPs) interconnected by bridging edges. AFRC displayed inverse correlation with mean coordination number and system energy, with sigmoidal dependence capturing the progression from reconfigurable to stable states. Notably, we discovered a "Goldilocks regime" in which structural complexity maximizes functionality: The peak near infrared backscattering intensity (at 820 nm) occurred precisely when ORC reached its minimum at ~120 s, corresponding to interconnected mesocrystals with low symmetry. This intermediate state, combining order and disorder, produced 40% higher plasmonic response than either fully dispersed particles or perfectly ordered superlattices. The generalizability of the GT framework was demonstrated across three NP systems: gold nanocubes forming rhombic lattices, gold nanoprisms assembling into hexagonal superlattices through liquid-like nanocolumn intermediates, and indium tin oxide nanospheres forming either crystalline clusters or kinetically trapped gels depending on interaction strength.

CONCLUSION: The GT metrics, such as ORC and AFRC, provide continuous measures of global connectivity patterns and local energetic states throughout dynamic self-assembly processes, capturing features invisible to conventional order parameters. Most importantly, ORC quantifies effective complexity in NP assemblies, enabling experimental validation of decades-old theoretical predictions that functionality peaks at intermediate complexity states combining order and disorder. The framework provides a path forward for designing and controlling complex nano- and microstructured materials with properties that emerge from the interplay between local order and global connectivity, advancing applications in biosensing, photonics, and lightweight nanomaterials. □

Corresponding authors: Thomas M. Truskett (truskett@umich.edu); Delia J. Milliron (milliron@umich.edu); Qian Chen (qchen20@illinois.edu); Xiaoming Mao (maox@umich.edu); Paul Bogdan (pbogdan@usc.edu); Nicholas A. Kotov (kotov@umich.edu) †These authors contributed equally to this work. **Cite this article as J. Hallstrom *et al.*, *Science* 392, eaeb5134 (2026). DOI: 10.1126/science.aeb5134**

NANOPARTICLE ASSEMBLY

Decoding collective dynamics and complexity in nanoparticle assemblies using graph theory

Jonas Hallstrom[1,2]†, Puquan Pan[2,3]†, Jayson Sia[2,4]†, Sangwok Bae[2,5,6], Dingwen Qian[7,8], Chang Qian[3], Sindy Liu[3], Lehan Yao[3], Thomas M. Truskett[5,7,8]*, Delia J. Milliron[7,8]*, Qian Chen[2,3]*, Xiaoming Mao[1,2]*, Paul Bogdan[2,4]*, Nicholas A. Kotov[2,5,6,7]*

Being intermediate in scale between molecules and colloids, nanoparticles combine characteristics of both. The structure of their self-assembled states combining order and disorder is difficult to quantify using traditional symmetry-based descriptors. Here, we applied graph theory (GT) to analyze assemblies of 400 to 10,000 nanoparticles across three material systems. We show that GT metrics, augmented Forman-Ricci curvature (AFRC) and Ollivier-Ricci curvature (ORC), capture local and global structural transitions from small clusters to extended networks. AFRC reflects the energetic state of the assembly, whereas ORC quantifies structural complexity and reveals a "Goldilocks" regime that maximizes plasmonic response. The generality of this approach is demonstrated for gold nanocubes, gold nanoprisms, and indium tin oxide nanospheres, providing a unified framework for describing and optimizing complex nanoparticle assemblies.

The physical dimensions of inorganic nanoparticles (NPs) place them between molecules and colloids, giving rise to self-assembly behaviors analogous to but also fundamentally distinct from particles at smaller and larger scales (*1*–*5*). The interaction potentials of molecules in solutions, driving their self-organization, encompass quantum effects and are highly orientation dependent. Their thermal energy, k_BT, is comparable to the energy of intermolecular interaction. Combined with rapid molecular diffusion and extensive sampling of configurations, molecular assemblies produce highly ordered structures, either dense crystals or porous frameworks, simplifying the description and prediction of emerging structures. By contrast, micrometer-sized colloidal particles exhibit much slower diffusion times and shorter ranges of interaction compared with particle size. Their interaction potentials are mostly isotropic, which again favors a few simple symmetric crystal lattices (*6*–*8*), and their thermal energy often cannot overcome close-range interparticle interactions, resulting in stochastic flocculation determined by collision-limited sticking rather than thermal equilibration. Interparticle potentials for NPs are deeper and simpler than those for molecules, but they remain nonisotropic because of molecular anisotropy of surface ligands (*2*, *9*). NPs exhibit rapid Brownian dynamics, but not as fast as molecules, which limits their reconfigurability. Although they are capable of crystallization, gelation, and flocculation, they also produce a wide range of highly complex structures combining order and disorder due to the unique behavior intermediate between molecular chemistry and colloid science.

These differences are particularly important for the formation of technologically attractive low-density two-dimensional (2D) films and 3D solids when NPs form chains, clusters, and pores (*5*, *10*). The organization and dynamics of these types of structures are strongly affected by the dispersions of NPs in shapes and compositions (*11*), kinetic traps (*12*, *13*), and their dynamic reconfiguration (*14*). Deciphering the complexity and cooperativity of NP interactions is also relevant for dense NP solids, the formation of which also deviates from the crystallization pathways known for molecules and colloids (*15*–*17*). Both the transient states and final structures are strongly affected by reconfigurable surface ligands (*2*, *18*–*20*) and long-range repulsion (*1*, *21*, *22*), leading to low-density packings (*23*, *24*) with a variety of intricate organizational patterns.

The common order parameters and theories previously developed for crystals are problematic for describing partially organized NP systems. For example, it is easier to quantify even small structural changes in regular NP crystals (*15*, *25*, *26*) than big changes in largely irregular and often heterogeneous NP gels (*27*–*29*). The current order parameters for crystals, glasses, and mesoscale states, which range from simple descriptors such as coordination numbers to more complex descriptors such as bond order parameters, cannot adequately identify structural organization without partial translational or rotational symmetry, regularity, or self-similarity (tables S1 and S2) that is typically absent in most of the practically made self-assembled nanostructures. A general methodology to quantitatively describe low-order and low-density states is also important for applications that exploit optical, mechanical, and electrical properties controlled by defects and hierarchy of the reconfigurable assemblies (*30*–*32*). Even with the constantly expanding collection of machine learning and artificial intelligence tools, one cannot design, optimize, or (re)produce materials with structures that one cannot quantify.

We used a graph theory (GT) (*33*, *34*) framework for the characterization of dynamic NP systems undergoing the transition from dispersions of free NPs to fully assembled colloidal crystals. Wide-frame time-resolved liquid-phase transmission electron microscopy (LPTEM) (*4*, *25*) enabled us to extract graphs capturing complex dynamics of >400 NPs distributed over a large area in real time, and molecular dynamics (MD) and kinetic Monte Carlo (kMC) simulations allowed us to study dynamic particle systems consisting of 10,000 NPs and dozens of intermediate mesoscale crystals. We demonstrate that the GT parameters captured essential structural features in the dynamical reconfiguration of NP assemblies. They also established relations between complexity and functionality that allowed us to identify the extrema of plasmonic effects.

Dynamic structural graphs from time-resolved electron microscopy in liquids

As the primary experimental model, we used dispersions of corner-truncated gold nanocubes (edge length $L_e = 63.3 \pm 5.2$ nm, edge truncation $L_t = 17.1 \pm 1.2$ nm) (Fig. 1A) bearing ionizable long-chain carboxylate-terminated thiols [$HS(CH_2)_{11}(OCH_2CH_2)_6OCH_2COOH$] that undergo long-range electrostatic repulsions in water. Their dynamics at the single-particle level were captured by LPTEM (*4*). Prior studies showed that these and similar NPs can form highly ordered superlattices with rhombic symmetry, the assembly of which can be triggered by flowing phosphate buffered saline (PBS, pH 8, $I = 15$ to 26 mM; see the materials and methods) inside the liquid cell (Fig. 1, A and B, and movies S1 and S2) due to strong van der Waals attraction overrunning screened electrostatic repulsion (*17*, *35*). Because the bond angles in this NP lattice vary between 60° and 90°, conventional local bond orientation order parameters for square (ψ_4) or hexagonal (ψ_6) lattices (tables S1 and S2) falsely characterized the final assembly as a low-crystallinity

[1]Department of Physics, University of Michigan, Ann Arbor, MI, USA. [2]Center for Complex Particle Systems (COMPASS), University of Michigan, Ann Arbor, MI, USA. [3]Department of Materials Science and Engineering, Grainger College of Engineering, University of Illinois, Urbana, IL, USA. [4]Viterbi School of Engineering, University of Southern California, Los Angeles, CA, USA. [5]Biointerfaces Institute, University of Michigan, Ann Arbor, MI, USA. [6]Department of Materials Science and Engineering, University of Michigan, Ann Arbor, MI, USA. [7]Department of Chemical Engineering, University of Michigan, Ann Arbor, MI, USA. [8]McKetta Department of Chemical Engineering, University of Texas at Austin, Austin, TX, USA. ***Corresponding author. E-mail: truskett@umich.edu (T.M.T.); milliron@umich.edu (D.J.M.); qchen20@illinois.edu (Q.C.); maox@umich.edu (X.M.); pbogdan@usc.edu (P.B.); kotov@umich.edu (N.A.K.)**
†These authors contributed equally to this work.

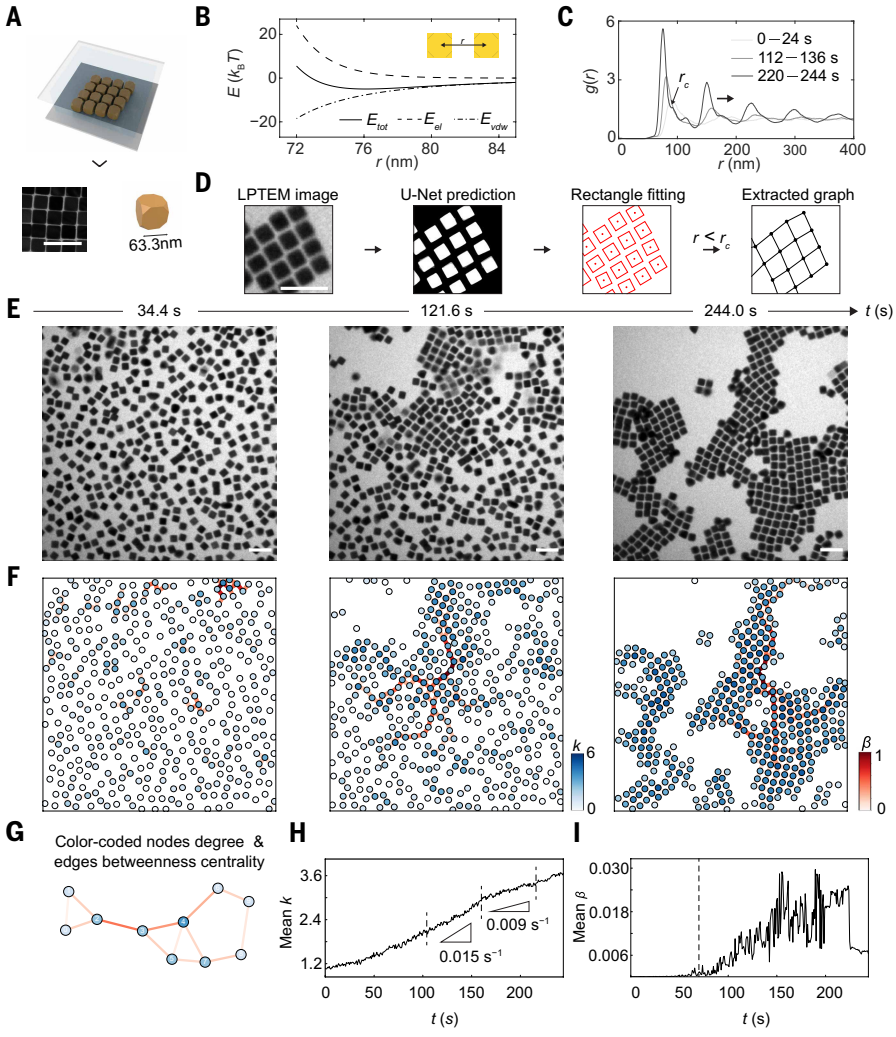

Fig. 1. GT analysis of reconfigurations of NPs during their self-assembly. (**A**) Schematic of gold nanocubes and their colloidal crystals. (**B**) Pairwise interaction energy of two gold nanocubes approaching in face-to-face alignment. (**C**) Radial distribution functions of NPs at three stages of self-assembly. We applied periodic boundary correction (*76*) to extract the $g(r)$ so that the limited size of the lattice would not affect the $g(r) - r$ profile. (**D**) Graph construction workflow from the LPTEM movies. (**E**) Snapshots of the LPTEM movies of NPs transitioning from fully disordered to fully ordered states. Scale bars, 200 nm. (**F**) Graph representation of the corresponding frames with node and edge colored according to the values of degree and betweenness centrality, respectively. (**G**) Schematic illustrating varying nodal degrees and edge betweenness centrality values. The numbers in the circle label different particles. (**H**) Temporal progression of mean degree with distinct stages corresponding to a slope of 0.015 s^{-1} observed before $t = 160$ s, followed by a state with a slope of 0.009 s^{-1}. (**I**) Temporal progression of mean betweenness centrality, β.

state. The classical radial distribution function $g(r)$ with multiple peaks (Fig. 1C) revealed a high degree of organization of the final assembly with bond length l (e.g., $l = 75.9 \pm 5.4$ nm at $I = 26$ mM) and a bimodal distribution of the bond angles θ (peaking at θ = 75.5° and 103.2°) (figs. S1 to S3).

Analysis of the transient states between free-particle dispersions and densely packed superlattices was performed with an image segmentation workflow (*36*) based on the U-Net convolutional neural network extracting binary masks of nanocubes in each frame (Fig. 1D and figs. S4 and S5). The system states observed during the reconfiguration processes were described by graphs generated by assigning nodes to the NP centroids with positions calculated in each frame (see the materials and methods). Two NPs were considered as interacting and thus connected with an edge if they were less than r_c apart, where r_c is 1.15 times the distance corresponding to the first peak of $g(r)$ (Fig. 1C, figs. S6 and S7, and supplementary text). The collection of all graphs obtained for different assembly times produced time-dependent (dynamic) graphs (*37*) characterizing the entire system transitioning from the state of randomly dispersed NPs to a fully assembled crystalline state.

GT parameters for short- and long-range structural patterns

Dispersed NPs can produce states that combine regularity, fractality, and stochasticity (*24*, *28*), which requires a new mathematical toolbox for their description. Prior applications of GT and network science (*38*) demonstrated their efficacy in revealing hidden yet repeatable patterns characteristic of social media (*39*), infection transmission (*40*), and geological events (*41*), but this toolbox of discrete mathematics has only recently been applied to descriptions of complex (nano)materials combining order and disorder (*42*). Although GT analysis has been insightful for understanding seemingly random organization of nanotubes (*43*), nanofibers, (*42*) organic molecules (*44*), polymers (*45*), nanogels (*28*), and polymer films (*46*), these studies were focused on static structures and did not address their dynamics.

Various short- and long-range correlations between NPs can be captured and evaluated unambiguously by the suite of GT parameters. We initially considered nodal degree, k (also referred to simply as degree), and edge betweenness centrality, β, that describe short- and long-range structural patterns in NP systems, respectively (Fig. 1, E and F). Physically, k is the number of edges incident onto a node. It corresponds to several nearest neighbors no farther than r_c from a specific NP; it is analogous to structural parameters of bond order and valency. In the same vein, β quantifies the importance of an edge in global connectedness of the network, which has no counterpart in the existing library of materials order parameters. It is defined as the ratio of the number of shortest paths between pairs of nodes that go through a specific edge and the total number of shortest paths in the system.

Considering the dynamics of corner-truncated gold nanocubes, a nearly disordered initial state is composed of single particles, pairs, and a few clusters. Such a nanosystem displays a mean degree close to 1 obtained by averaging nodal degrees of all NPs in each frame. The mean degree of all the nodes in each frame steadily increases to 3.6, nearing 4 in the end state, a characteristic k for a 2D rhombic lattice (*47*). The temporal dependence of mean degree shows mild sigmoidal dependence (Fig. 1, G and H), and the variable $\partial k/\partial t$ gradient suggests a transient state between 70 and 150 s of the assembly at time t. Compared with molecules, this state is analogous to the atomic configurations, with unusual valences corresponding to the transient states in chemical reactions.

During the first 70 s, β stays near zero, which reflects the limited connectivity between the NPs (Fig. 1I). After 70 s, β starts to increase but its growth remains nonmonotonous. Large fluctuations emerge because β is highly sensitive to edge connection and disconnection

(Fig. 1I). Coinciding with the decrease in $\partial k/\partial t$ shown in Fig. 1H, the fluctuations increase substantially at t ~150 s. Although the use of β was successful in capturing phase transitions in the past (*48*), these fluctuations make structural analysis difficult, which highlights the differences in molecular and colloidal systems and NP dispersions and the importance of concerted reconfigurations of particles in the latter. Note also that these fluctuations originate from the attachment and detachment of NP clusters, which points to the central role of concerted reconfiguration of multi-NP segments for evolution from random to crystalline states.

Global transient state and Ollivier-Ricci curvature

The limitations of common graph metrics in analyzing the structures formed by NPs and the lack of periodicity and symmetry in transient states of NPs prompted the exploration of alternative measures for characterizing the reconfiguration of the system as a whole. Ollivier-Ricci curvature (ORC) is an adaptation of Riemannian geometry for continuous objects to discrete point sets forming graphs (*49*). For complex materials and chemical systems, ORC quantifies how local mechanical, thermal, or chemical interactions propagate in the wide neighborhood of an edge, thereby capturing collective behavior of multiple particles. Compared with order parameters (e.g., coordination number and bond order) and other GT descriptors (e.g., k) used previously, ORC captures the organization of networks beyond the nearest-neighbor distance, reflecting connectivity patterns of the next-nearest-neighbors and next-next-nearest-neighbors (Fig. 2A). With values of ORC for individual edges always spread between −2 (extreme bottleneck) and 1 (multiple redundant paths), ORC >0.25 indicates the presence of the formation of size-limited subgraphs with strongly interconnected nodes (Fig. 2, A and B). ORC ~0 indicates a "flat" graph with evenly distributed connections that is often seen in grid-like or regularly spaced networks such as the square lattice. ORC <−0.25 indicates edges that serve as "bridges" between otherwise separate communities. Thus, ORC captures the complex mesoscale features emerging during the NP assembly processes. This metric, therefore, characterizes the pattern of collective interactions and dynamics beyond the single-NP level, a structural descriptor that was lacking in the sets of both traditional order parameters and simple GT descriptors.

Unlike k and β, the average ORC does not increase or decrease monotonically but has a minimum value during an intermediate stage of the assembly process, dividing it into three stages (Fig. 2, C to E). The initial stage (0 to 60 s) exhibits a near-zero ORC reflecting the state when most particles are disconnected, which in fact matches the stage of β ~0 in Fig. 1I. The second stage corresponds to strongly negative ORC and the formation of medium-sized, dynamically reconfigurable clusters of NPs. They can be referred to as mesocrystals, i.e., groups of 4 to 20 NPs that are not only within the separation threshold r_c but also have an aligned relative orientation within 10° of their neighbor, which is characteristic of the superlattice. In GT terms, these partially organized intermediates correspond to subgraphs containing at least four but <20 nodes. The 60 to 120 s stage reflects the formation of NP-NP edges bridging the mesocrystals; these edges display large negative values of ORC that make the global ORC also negative. The minimum in ORC curve coincides with the highest occurrence of

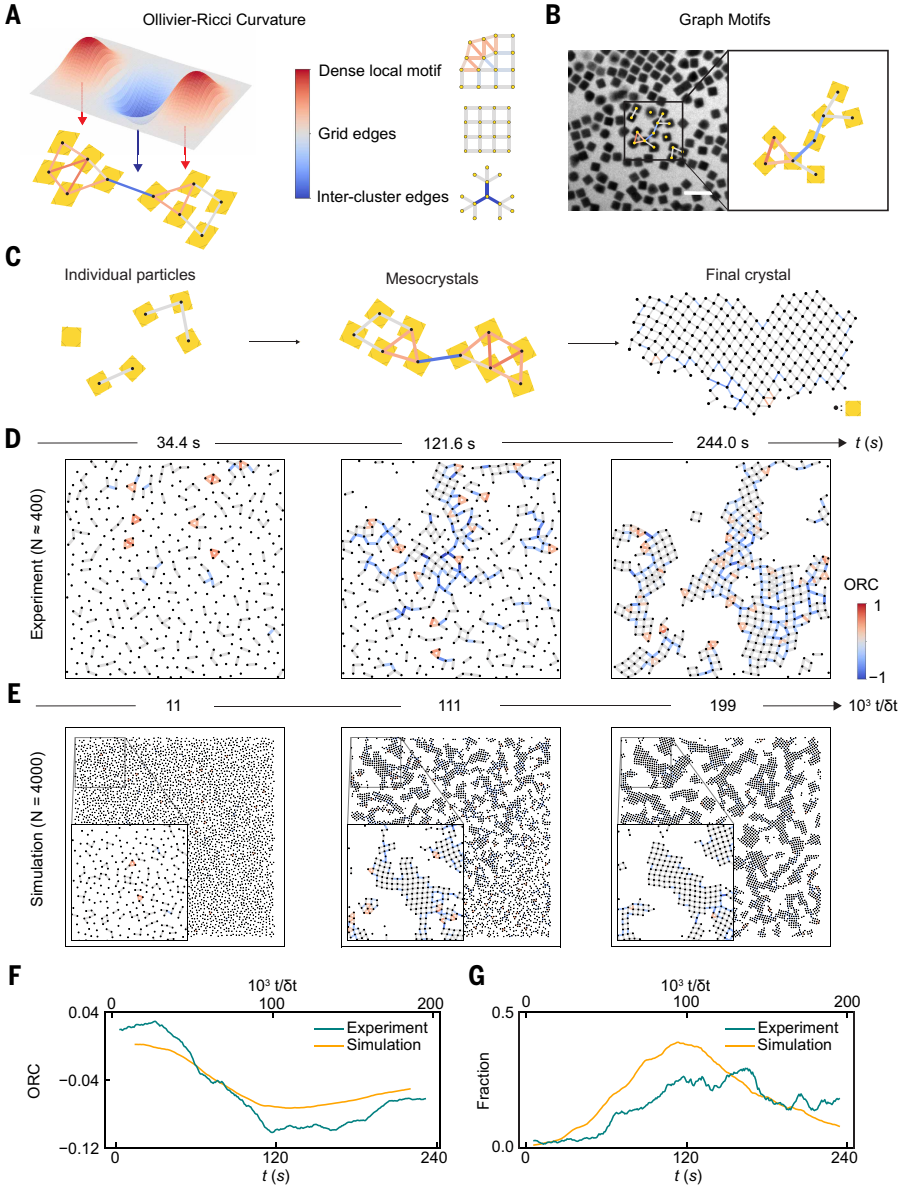

Fig. 2. ORC characterizes global complex organization of NP systems with order and disorder. (**A**) Analogy between manifold curvatures and ORC. The height is related to ORC values. (**B**) Graph motif taken from a LPTEM snapshot with edges color coded to ORC values. Scale bar, 200 nm. (**C**) Illustrations of the multistep assembly process. White edges corresponding to ORC = 0 occur when a system produces a "regular" pattern consistent with Bravais lattices, such as square, rhombic, or hexagonal crystals. Red edges or positive ORC happen when the local area around an edge is more connected and has more 3-cycles than its surroundings. (**D**) Snapshots of NP positions for LPTEM images over time (seconds). (**E**) Snapshots of NP positions for MD-simulated assemblies (time steps). Snapshots in (D) and (E) were chosen to be at their highest mean ORC, lowest mean ORC, and final frame, with edge color showing ORC. (**F**) Progression of smoothed mean ORC for the configurations of NP system observed in the LPTEM and MD simulations. Minima are at ~120 s and ~100,000 time steps, respectively. (**G**) Evolution of the NP system based on the particle fraction in medium-sized mesocrystals.

medium-sized mesocrystals (Fig. 2, F and G, and figs. S8 and S9) and bridges between them (figs. S10 and S11). Such dynamics highlight the ability of ORC to capture both the local (i.e., formation of mesocrystals) and the global (i.e., their connectedness throughout the system) organization of the dispersion. At the final stage (after 120 s), the mean ORC increases and approaches zero as mesocrystals merge, becoming "flat" in the context of the Riemannian geodesics that correspond to the formation of continuous superlattice. Note that for practical systems, NPs located at the edges of crystalline domains and lattice imperfections can be both positive and negative ORC (Fig. 2, D and E) while being near perfect zero in the middle of the domains; this also highlights the importance of ORC maps for high-density NP solids.

Local transient states and augmented Forman-Ricci curvature

Although average ORC trajectories can effectively describe the global organizational patterns in mesoscale (500 to 1000 nm), it would be useful to capture the collective behavior of several NPs near each other undergoing simultaneous reconfiguration. The simplest arrangement of NPs beyond standard pair interactions are three-particle clusters that in GT terms are described as 3-cycles. The dynamics of 3-cycles capture multiparticle motions on the scale of 200 to 500 nm corresponding to the local reorganization in NP assemblies. Note that 4-cycles are the basic segments of the rhombic lattice, whereas 3-cycles are the deviations from the ideal packing in this lattice (Fig. 3A). Because they are energetically nonoptimal structures, 3-cycles are particularly important because they can serve as local transient states and can be used to track energy of the NP system.

To quantify abundance and connectivity patterns of 3-cycles during system reconfiguration, we used a new GT parameter, augmented Forman-Ricci curvature (AFRC; see the materials and methods), obtained by adding three times the number of 3-cycles formed by an edge to its Forman-Ricci curvature (FRC) (*50*). For material systems, this GT parameter quantifies local robustness of the network, with negative FRC corresponding to more stable structures and positive FRC corresponding to more reconfigurable structures. The modified version of FRC introduced here, AFRC, augments the contribution of triangular arrangements of NPs essential for multiparticle dynamics. AFRC increases with the total number of 3-cycles but decreases when fully connected 4-cycles are produced (Fig. 3B). For practically relevant NP systems with a limited number of neighbors, the AFRC values of edges will vary between –2 (stable lattices) and ~3 or 4 (states dominated by 3-cycles). Compared with the other geometric and topological descriptors mentioned above, AFRC extends the range of structural patterns without causing fluctuations as in Fig. 1I.

Altogether, these differences, along with computational efficiency, make AFRC particularly suitable for capturing the reconfigurability system through complex states. The sigmoidal dependence of AFRC along the self-assembly pathway indicates its correlation to the total energy of the NP system (Fig. 3, D and F). These points can be further supported by the fact that AFRC displays the opposite trend as mean degree, reaching a minimum for a strongly bonded fully assembled superlattice with limited ability to reconfigure (Fig. 3, E and G). To gain additional and independent confirmation of the AFRC relation to energy of the system, we extracted the graphs from the coarse-grained MD simulations description of 2D NP assemblies observed by LPTEM (Fig. 1E and see the materials and methods) based on "nanosquares" interacting through Lennard-Jones potential. This was validated by accurate descriptions of the interactions of gold nanocubes studied previously (see the materials and methods, note S2, and fig. S12). Additionally, our MD model containing 4000 NPs also allowed us to evaluate the effect of system size that can be significant for small networks (*51*).

The final rhombic lattice obtained in simulations (Figs. 2E and 3E) had structural parameters nearly identical to those of experimental superlattices, with a lattice constant of 79 nm and average rhombus cell angle of 79°. Furthermore, the simulated trajectories consistently replicated the experimental ones observed by LPTEM (movie S2 and figs. S8 to S12). For example, intermediate formation of mesocrystals from the initially disordered NPs was consistently observed; these interconnected mesocrystals then reconfigured until they merged into a superlattice.

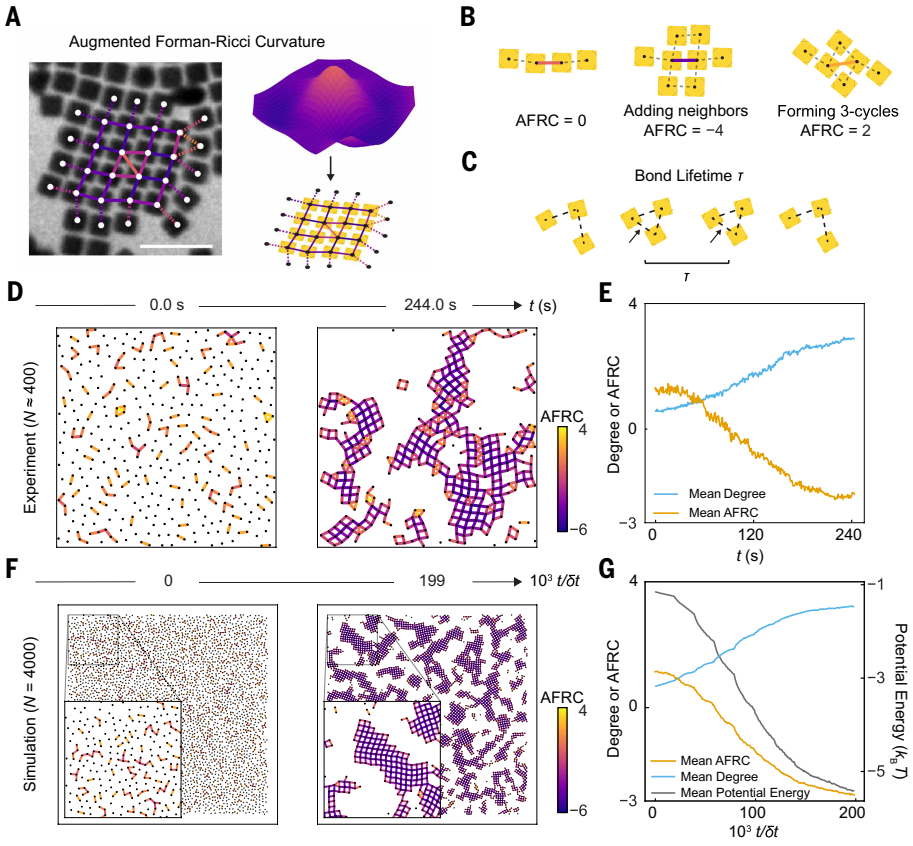

Fig. 3. AFRC characterizes the ability of the NP system to reconfigure producing local 3-cycle states. (**A**) Although 4-cycles represent the typical cell from the fully assembled superlattice, 3-cycles account for "defect" high-energy states enabling system reconfiguration. The height is related to AFRC values. Scale bar, 200 nm. (**B**) Schematics of local NP configurations and corresponding AFRC values of the solid edge. (**C**) Schematics for the calculations of edge lifetime, τ, and its relation to GT metrics. Experimental edge lifetime is calculated as the number of sequential frames observed in LPTEM during which two NPs are connected by an edge. (**D**) Maps of AFRC for the first and last frame of the LPTEM experiment. AFRC of each edge is shown in color according to the color bar on the right. (**E**) Mean degree and mean AFRC calculated for the NP assemblies observed in LPTEM. (**F**) Maps of AFRC for the first and last frame of MD simulations. AFRC of each edge is shown in color according to the color bar on the right. (**G**) Mean degree, mean AFRC, and potential energy were calculated for the NP assemblies observed in MD simulations.

The visual assessment of the trajectories was enhanced by the quantitative analysis of GT parameters. We calculated the Pearsons correlation coefficient, p_τ, between AFRC and the lifetime of edges (Fig. 3C), τ, in structural graphs obtained from MD simulation (*52*). A clear inverse correlation between AFRC and τ confirmed the propensity of edges with high AFRC to reconfigure (fig. S13). We also note that the values of p_τ for AFRC were much higher than for k with the edge lifetime, persisting over the entire trajectory, which confirms the significance of 3-cycles and the ability of AFRC to describe system reconfigurability. Finally, the strong anticorrelation between AFRC and mean degree observed in experimental structural graphs was reproduced with high fidelity in the simulated system (fig. S14), indicating that the size of the NP system in LPTEM was sufficient to establish the general relations to be observed for larger systems. This strong correlation between bond lifetime and AFRC highlights the importance of 3-cycles in reconfigurability, where information beyond immediate neighbors affects the breaking of bonds, and AFRC precisely characterizes this effect.

The experimentally measured ORC aligns with those obtained from MD simulations (Fig. 2F). It is less negative than that experimental ORC (Fig. 2F) because simulation did not have as high of a fraction of low-ORC "branching" structures and "bridging" edges (figs. S10 and S11). This difference is attributed to size variations of nanocubes, long-range interactions, and multibody effects not captured in simulations.

Optical properties of NP systems and complex assembly states

Although the plasmonic effects of metal NPs are well known, a methodology for quantitative description of the multiparticle states determining the plasmonic response at macroscale remains a challenge. These complex states emerge during self-assembly of NPs and are applicable to a variety of optical responses from dynamic nanosystems affected by short- and long-range interparticle interactions. To relate the GT analysis of NP dispersions to the macroscale observables, we calculated the scattering and backscattering spectra for 300- to 1100-nm wavelengths for NP configurations extracted from the LPTEM data (Fig. 4, A and B, and fig. S15). The peak intensities in the near infrared (NIR) range between 700 and 1000 nm deserve special attention because of their importance to (bio) sensors (*53*, *54*). These NIR peaks observed for backscattered photons are the ones responsible for a common functionality: the appearance of blue lines in a variety of flow assays, exemplified by pregnancy and COVID tests.

At $t = 0.0$ s of the assembly time, all optical properties of the NP dispersions were dominated by single NPs that displayed a strong plasmonic band at 550 nm without any peaks found in the NIR (Fig. 4, A, C, and H). The formation of small clusters (Fig. 4D), mesocrystals (Fig. 4E), and superlattices (Fig. 4, F and G) observed at later stages of the assembly process promotes collective plasmonic resonances between multiple particles, leading to the resonances in the NIR region (*55*). The tight packing of the NPs into fully ordered superlattices (Fig. 4G) results in broadening of the spectrum (*56*) and decreases the amplitude of the application-critical NIR bands in 800- to 850-nm window. The greatest backscattering, scattering, and extinction intensity (fig. S15) with optimal signal-to-noise ratio was observed at $t = 121.6$ s, when NPs formed complex systems of interconnected mesocrystals with low symmetry (Fig. 4E).

The progression of peak amplitudes and the timing of the maximal NIR scattering (Fig. 4B) matches closely the progression of ORC values and the timing of its maximum (Figs. 2F and 4B). This match is not coincidental, because the formation of interconnected mesoscale clusters resulted in minimal values of negative ORC and maximal scattering intensities, as can be demonstrated by the series of models shown in Fig. 4, C to G. Physically, this trajectory highlights the power of ORC to capture the dynamics of the network of multiple interactions in the NP system as a whole affecting its macroscopic physical properties. For example, the partially ordered NP systems with small, asymmetric, and interconnected clusters result in the maximal spectral shift that is favorable for biosensing and photonic applications (*53*, *54*, *57*).

Considering that GT provides mathematical tools for the quantification of complexity (*14*, *58*, *59*), NP assemblies offer a platform for examining the relations between complexity and functionality typical for biological materials hypothesized by several theoreticians >50 years ago (*60*–*62*). Using the terminology coined by Gell-Mann (*60*), the relation between effective complexity, EC, and functionality should follow a bell-shaped curve, peaking at the intermediate states combining order and disorder (fig. S16). Although intellectually appealing, the pathway to experimental substantiation of this hypothesis was not possible because experimentally accessible measures of EC were not available.

In this context, free NP dispersions and closely packed crystalline NP superlattices represent the two terminal states: fully disordered and fully ordered. NP dispersions with multiple partially ordered intermediate states with specific structural patterns but no periodicity offer a nearly ideal case for testing the theoretical relations of EC and materials functionality (fig. S16). The self-assembled structures shown in Fig. 1, E and F, and Fig. 2, D and E, represent the progression of intermediate states with correlated disorder. Furthermore, ORC

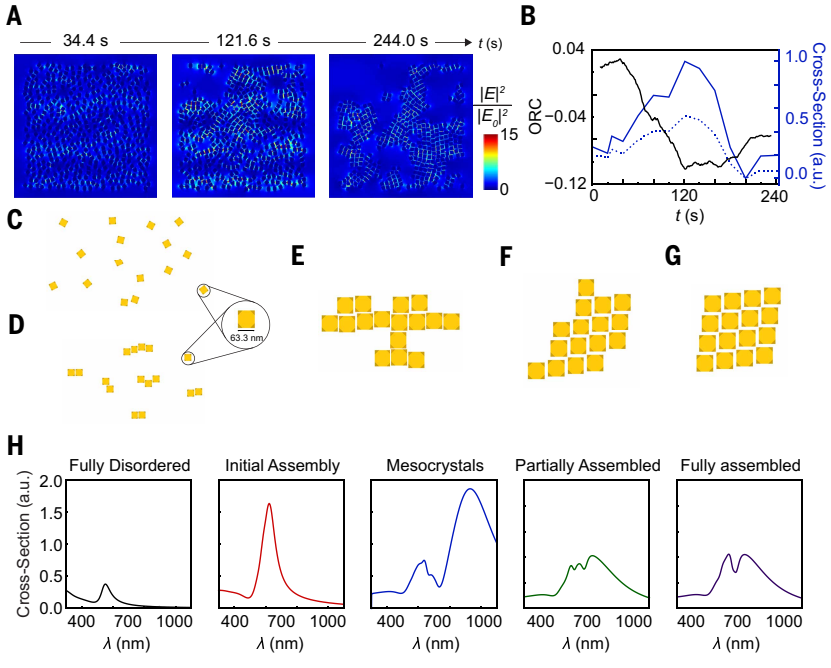

Fig. 4. Optical properties calculated using finite-difference time domain (FDTD) simulations. (**A**) Electric field intensity between gold NPs corresponding to the NP configurations observed in LPTEM at 34.4 s (predominantly singular NPs), 121.6 s (interconnected mesocrystals), and 244.0 s (continuous superlattice). (**B**) Scattering (solid blue line), backscattering (dashed blue line) cross-section plot (at 820 nm), and ORC (solid black line) for the NP configurations observed in LPTEM at different times. Peak is at ~120 s. (**C** to **G**) Configurations of Au nanocubes ranging from fully disordered NPs in dispersion (C), initial assembly states (D), interconnected mesocrystals (E), partially assembled superlattice (F), to fully assembled perfectly ordered superlattice (G), with the corresponding backscattering spectra shown in (**H**). The total numbers of NPs and their dimensions are identical for all configurations. a.u., arbitrary units.

provides a continuous measure of local and global organization of the system, whereas k and AFRC reflect the collective interactions and local transition states. The negative of ORC can therefore serve as a quantitative representation of EC. Indeed, ORC values are small for both fully ordered and fully disordered states. The negative ORC is at its maximum when NPs form a network of interconnected mesocrystals, representing an obvious case of order-disorder combination. Because backscattering resonances represent the key functionality of the dynamic systems from gold NPs, the "Goldilocks curve" for plasmonic scattering (Fig. 4B) following the trajectory of ORC completes the complexity-functionality relations analogous to those shown in fig. S16. It also demonstrates that the states observed for NP systems combining order and disorder do reveal greater functionality, as was hypothesized by Gell-Mann (*60*) and others (*61*, *63*, *64*).

Generalizability of GT-based analysis of assembly pathways

To demonstrate the generalizability of the GT framework beyond gold nanocubes, we applied it to the assembly of gold nanoprisms that undergo the transition from freely dispersed NPs to a hexagonal lattice made from nanocolumns (Fig. 5, A and B). Different from nanocubes, this NP system involves two complex intermediates characteristic of nonclassical crystallization pathways (*4*): (i) nanocolumns self-assembled from stacked nanoprisms misaligned around their short axis and (ii) a liquid-like state from the entire nanocolumns forming before the hexagonal superlattice.

The analysis of GT trajectories for the nanoprisms shown in Fig. 5, C and D, and fig. S17 demonstrates their similarity to GT trajectories for the nanocubes shown in Fig. 2F. Sparse graphs appropriately describe the initial stage (0 to 15 s) of the trajectory corresponding to the gas-like state of the system and its transition to the intermediate liquid phase (Fig. 5, A and C). The topology of the assembled structures in the intermediate stage (15 to 100 s), characterized by large cycles, is correctly identified by a negative mean ORC reaching the low extremum indicating the presence of the complex transient states mentioned above. In the crystallization stage (100 to 120 s), the system transitions from the dense liquid to the ordered solid. This transition involves the coalescence of liquid domains and the removal of "bridges" with negative ORC between them, which corresponds to a sharp, rapid increase in the mean ORC. In the final stage (>120 s), the large-scale crystalline phase stabilizes, causing the mean ORC to plateau near zero, reflecting a "flat" and highly ordered hexagonal graph. The trajectory for AFRC in fig. S18 also displays a trajectory like that for nanocubes shown in Fig. 3, E and G, and its connection to the total energy of the system. We can also use AFRC to identify local structural motifs corresponding to the liquid- and solid-like states (fig. S18A). As the columns form the liquid phase, which is a more connected graph with fewer 3-cycles, AFRC becomes more negative (fig. S18A). As the system crystallizes into a hexagonal lattice of the columns of the solid-like state, AFRC approaches ~−1.5, conforming to the expectations of a theoretical AFRC for a perfect, fully 3-cycle–based hexagonal lattice with each edge having AFRC = 4 − 6 − 6 + 3*(2) = −2, as shown in fig. S18B, a visualization of the distribution of the different phases. This steady decrease of AFRC (fig. S18C) captures the increasing stability of the system and decrease of its potential energy, consistent with our observations with the nanocubes (Fig. 3E). The transitions from a liquid-like state to a solid-like state can be also identified using the number of edges corresponding to the liquid- and solid-like states (fig. S18D). A solid cluster emerges beyond the cluster size of ~250 highlighting the liquid-solid transition, which demonstrates the capabilities of the GT approach.

The second NP system we considered involves self-assembly of freely dispersed spherical tin-doped indium-oxide (ITO) NPs into a gel (*65*).

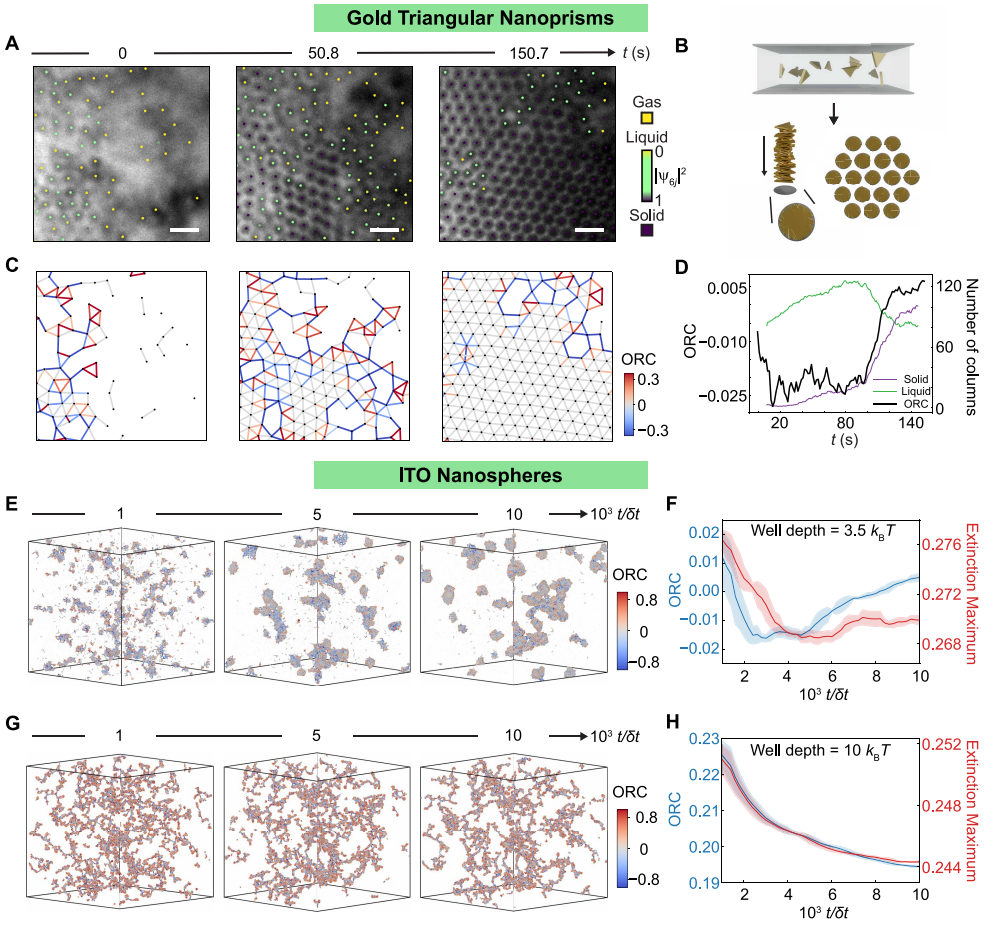

Fig. 5. Generalizability of ORC-based assembly pathway analysis. (**A**) TEM snapshots obtained from supplementary video 4 of (*4*) for the real-time self-assembly dynamics at 0, 50.8, and 150.7 s, with nanoprism columns colored according to $|\psi_{6j}|^2$: gas-, liquid-, and solid-like states of nanocolumns are colored yellow, blue and red, respectively. Time stamps are given above the TEM images. Scale bars, 200 nm. (**B**) Schematics of the hexagonal lattice self-assembled from gold triangular nanoprisms. (**C**) Graph representations of TEM images in (A) with edges colored according to ORC. (**D**) Trajectory of smoothed mean ORC for the configuration of nanocolumns (black, left ordinate) and the numbers of liquid- (green) and solid-like (purple) columns from (*4*). (**E** and **G**) Simulations of 10,000 ITO nanospheres undergoing assembly at attraction strengths of 3.5 k_BT (E) and 10 k_BT (G) shown at 1000, 5000, and 10,000 time steps, with edges colored by ORC. (**F** and **H**) Smoothed trajectories of the mean ORC (blue, left ordinate) and the spectral maximum of the extinction efficiency of the clustered particles (red, right ordinate) for the 3.5 k_BT (F) and 10 k_BT (H) simulations shown from time steps 1000 to 10,000. Shaded regions denote SDs computed over a 1000–time step window.

This system was chosen as a test case both for being a fully 3D system and for having plasmonic effects like those of gold NPs (Fig. 4). We analyzed kMC simulations and optical properties as described and validated through experimental data in (*29*), where NPs interact through a short-ranged isotropic attraction of tunable strength, ε.

Figure 5, E and G, compare two cases with $\varepsilon = 3.5\ k_BT$ and $\varepsilon = 10\ k_BT$, corresponding to systems that form local crystalline clusters and a complex globally connected gel-like network, respectively. The difference between these structures was also borne out in the average ORC trends over time. The structure with mostly crystalline clusters had an average close to zero (Fig. 5, E and F). The gel-like structure had a significantly positive ORC due to the thin filaments of the gel having an excess of 3-cycles and densely connected neighborhoods that do not exist in a bulk crystal (Fig. 5, G and H).

Similar to gold nanocubes, we found qualitative correlations between a system's ORC and optical properties over time. We calculated the spectral maximum of the extinction efficiency for the clustered particles over the course of the ITO NP simulations. Comparing the extinction maximum trajectory with the ORC trajectory in the $3.5\ k_BT$ simulation (fig. S19) revealed a minimum mirrored by the trajectory for optical extinction (Fig. 5F). Note that the behavior of ORC was fundamentally different when the energy of particle attraction was 10 times the thermal energy, i.e., $\varepsilon = 10\ k_BT$, corresponding to rapidly flocculated (nano)colloids. Remaining always positive, ORC monotonically decreased over time without a maximum in this case, reflecting the gradually increasing complexity while retaining the same structural motif. The monotonic ORC trend was mirrored by a monotonically decreasing trajectory for extinction maximum (Fig. 5H). This comparison demonstrates the ability of ORC to distinguish between self-assembly pathways leading to crystalline clusters and kinetically trapped gels.

In conclusion, taking advantage of real-time, real-space data on NPs transitioning from low-density freely dispersed states to closely packed crystalline states, this work addresses the problem of structural description of partially disordered particle systems. We performed GT analysis of large NP systems comprising up to several thousand particles, not assuming their symmetries or self-similarity. As a result, we showed that (i) GT parameters can be successfully used for quantifying both local and global structural changes throughout the self-assembly process and (ii) the collective movements of small clusters of a few NPs rather than individual particle dynamics define the assembly pathway. The development of new metrics for continuous assessment of structural organization of NP systems from fully ordered to fully disordered states made it possible to quantify the effective complexity hypothesized in prior theoretical studies, which reflects the functionality of the material.

The proposed GT parameters offer a framework generalizable to multiple other dispersions of nanoscale particles. Similar approaches can also be useful for solids, slurries, and dispersions from molecular, mesoscale, and microscale particles that can be characterized as high-entropy materials with correlated disorder. Additional work is needed to explore other particle systems with 2D and 3D lattices with a range of degrees and symmetries. More complex assembly pathways and structures can also be expected for highly anisotropic NPs, which are likely to enrich our knowledge about intermediate states and high-complexity materials.

Materials and methods

Chemicals

Sodium borohydride (99%, Sigma-Aldrich), silver nitrate (≥99.0%, Sigma-Aldrich), *L*-ascorbic acid (BioXtra, ≥99.0%, Sigma-Aldrich), hexadecyltrimethylammonium bromide (BioXtra, ≥99%, Sigma-Aldrich), gold (III) chloride trihydrate (≥99.9%, Sigma-Aldrich), hexadecylpyridinium chloride monohydrate (>98.0%, TCI), sodium phosphate monobasic monohydrate (99.0 to 102.0%, EMD Millipore), sodium phosphate dibasic anhydrous (99%+, Acros), potassium bromide (99.999%, Acros), hydrochloric acid (99.999%, Alfa Aesar), sodium oleate (> 97%, TCI), and 2-(2-[2(11-mercapto-undecyloxy)-ethoxy]-ethoxy)-ethoxy-ethoxy-acetic acid (≥ 95%, $HS(CH_2)_{11}(OCH_2CH_2)_6OCH_2COOH$, Prochimia Surfaces) were used as purchased without further purification. All glassware was treated with aqua regia (a mixture of HCl and HNO_3 with a volume ratio of 3:1), thoroughly rinsed with water, and dried before use. Nanopure water (with a resistivity of 18.2 MΩ cm at 25°C) purified by a Milli-Q Advantage A10 system was used in this work.

Gold nanocube synthesis and surface modification and LPTEM sample preparation and imaging

Gold nanocubes were synthesized with adaptations to a universal seeded growth method (*4*, *25*, *66*). The synthesis includes three steps: (i) preparation of gold nanorods, (ii) preparation of monodisperse spherical seeds from the gold nanorods by iterative etching and regrowth, and (iii) growth of the gold nanocubes from the monodisperse spherical seeds. The gold nanocubes obtained above were coated with hexadecyltrimethylammonium bromide (CTAB) ligands. The ligands were exchanged with carboxylate-terminated thiols ($HS(CH_2)_{11}(OCH_2CH_2)_6OCH_2COOH$) following literature procedures (*36*) to improve the stability of the NPs in solution. LPTEM imaging was performed using a Hitachi 9500 TEM with a LaB_6 emitter at 200 kV and an electrochemical liquid flow TEM holder (Hummingbird Scientific). The SiN_x microchips used in our experiments were purchased from Hummingbird Scientific (200-nm spacer microchip with a window size of 50 μm × 200 μm × 50 nm; rectangular top microchip with a window size of 30 μm × 650 μm × 50 nm). Right before the microchip assembly, the flow tubing was wetted with water and the microchips were treated with oxygen plasma (Harrick Plasma Cleaner PDC-23G) at a low radiofrequency (RF) level for 27 s to clean their surfaces and render them hydrophilic. LPTEM imaging was performed at low electron dose rates (11.2 to 15.4 $e^- Å^{-2} s^{-1}$) to minimize beam-induced reactions and to preserve inter-NP interactions (figs. S1 and S2). Also, extensive prior testing indicated minimal beam-induced reactions and impact on NP behavior (*36*). The LPTEM movies (movies S1 and S2) were captured with a Gatan Orius fiber-optically coupled CCD camera with an exposure time of 0.1 s per frame at a rate of 10 fps. During postprocessing, for movie S1, we chose one frame every eight frames so that the final frame rate was 1.25 fps; for movie S2, the frame rate was not processed and was 10 fps.

Particle tracking

For the NP tracking, to train the U-Net model, we first generated a large dataset of simulated LPTEM images that served as the input, along with their corresponding ground truth masks (fig. S4). 3D models of the nanocubes were constructed based on the geometry and polydispersity observed in experimental TEM images (Fig. 1). These models were then placed in random positions with random in-plane orientations. From these 3D models, an NP thickness map was calculated for each simulated image (fig. S4B). Based on the thickness map, we could obtain the ground truth for training. Then, this map was blurred by filtering it with a disk filter. This step replicates the loss of sharpness caused by defocusing and electron scattering from the liquid and SiN_x windows in experimental LPTEM data.

Next, the blurred thickness maps were used to calculate the pixel intensities by applying the Beer-Lambert law:

$$I = I_0 e^{-\sum_i \frac{t_i}{\lambda_i}}$$

where I and I_0 are the transmitted and incident beam intensities, respectively, and t_i and λ_i represent the thickness and inelastic mean free path, respectively, for each species i (e.g., NP, water, and SiN_x window)

along the electron beam path (fig. S4A). To further mimic experimental conditions, shot noise, which follows a Poisson distribution relative to the electron dose rate, and readout noise, which follows a Gaussian distribution added to match the noise levels from the detector readout, were included. Finally, the simulated images were multiplied by the modulation transfer function derived from experimental LPTEM images. This step reproduces the nearby-pixel correlations observed in experimental data, improving the trained network's performance. (fig. S4B).

This simulation workflow generates the training and validation datasets needed to effectively train the U-Net model (fig. S4C). Once trained, the model was applied to experimental LPTEM movies. The raw TEM images were cropped into smaller blocks as input for the U-Net. The resulting predictions were combined into a single binary image for each frame and postprocessed by built-in Matlab functions of *watershed.m*, *regionprops.m*, and a rectangle-fitting algorithm. After that, the position of each nanocube and their orientation could be obtained.

MD simulation

All simulations were implemented as 2D MD simulations in HOOMD-blue (*67*). Only one type of simplified "nanosquare" was used in all simulations, a rigid body containing 25 point-particles arranged in a square grid that interacted with other such particles through a Lennard-Jones potential. Taking the simulation length unit as nanometers to be analogous to the experiment, the simulated nanosquares had an edge length of 50 nm, and the Lennard-Jones interactions of the constituent point particles had a σ of 26.5 nm and an interaction cutoff at 100 nm. The minimum energy configuration for two such nanosquares is to be closely aligned at a separation of 78 nm, and the minimum energy configuration for a small rhombic lattice of 2 by 2 units cells is to have a rhombic cell of length 78 nm and small angle of ~79° (fig. S7 and supplementary text).

For the system settings, all simulations initialized particles in either a square or hexagonal grid with random orientations at a density of 8×10^{-5} particles/nm^2. These simulations then underwent a short "randomizing" simulation, where the Lennard-Jones interactions were cut off to only include the repulsion at short distances and the NPs moved around for a short time without attracting or assembling. All simulations were also run at a temperature of $k_BT = 0.5$ energy units, where the nanosquares have a Lennard-Jones epsilon of 0.13 energy units and the strongest bond between two nanosquares is −3.7 energy units. This temperature was chosen simply because it was somewhat below the observed simulation crystallization temperature of ~$k_BT = 0.7$. All simulations were based on the Langevin equation of motion, and those shown here used friction coefficients of $\gamma = 0.1$ and $\gamma_r = 0.1$.

The first simulation used in most of the data presented here, including those in Fig. 2, D and F, Fig. 3, middle column, and Fig. 4, B to D, is the so-called wavefront simulation. This simulation, in addition to the parameters discussed above, also strongly inhibited the motion of the nanosquares until a plane wavefront moving from the top left to the bottom right released them to move more freely. This type of simulation was made to more closely be analogous to the experiment, which began with NPs strongly attached to their current dispersed position and then had the rotational and translation movements of those particles many times increased as the assembly progresses from the one corner of the LPTEM movie to the other. To implement this in simulation, we tried increasing the γ coefficients of the inhibited particles by 1000× until they were freed by the wavefront and increasing the mass of the particles by 500× until they were freed, with both implementations leading to similar results. In the simulation used in the above figures, the γ and γ_r coefficients of the inhibited particles were multiplied by 1000 until they were freed by the wavefront, and the wavefront had an angle of 45° and moved from the top left to the bottom right at a uniform speed. In the first 20 frames, all nanosquares were inhibited, then the wavefront spread at a uniform speed in several stages until all particles were uninhibited at frame 160, and from frame 160 through 210, all particles remained uninhibited. This speed was chosen to be comparable to experiment, where about half the particles appeared to be uninhibited in their rotational and translation movements by about halfway through the total number of frames (Fig. 2).

The second simulation was a more simplified and general scenario in which there were no gradients or waves affecting the system inhomogeneously like the experiment and wavefront simulation, but rather all nanosquares were uninhibited immediately and assembly commenced everywhere instantaneously.

The results shown in Figs. 3 and 4 were found to be largely consistent in further wavefront simulations, with k_BT values ranging from 0.4 to 0.7, γ values ranging from 0.01 to 1, γ_r values ranging from 0.01 to 10, and wavefront travel times ranging from instantaneous to 280 frames (280,000 time steps). Figures and data for these additional simulations are provided in the supplementary materials (supplementary text and figs. S8 and S9).

Graph construction

Based on the tracked centroid positions of NPs obtained from particle-tracking method described above, we first quantified the rhombic positional order in each frame of LPTEM movies using the radial distribution function $g(r)$ of the lattice as a function of r, the center-to-center distance of the NPs. $g(r) - r$ was calculated for the rhombic lattice consisting of all the NPs tracked in the final frames of the movie. From the first peak of $g(r)$, we defined a threshold r_c as 1.15 times this first peak or first nearest-neighbor distance. When $r < r_c$, we considered the two nanocubes as nearest neighbors linked by a bond. These nearest-neighbor relationships were used to construct a graph representation of the NP assembly. In this graph, each NP is represented as a node, and a bond between two NPs, defined by the condition $r < r_c$, is represented as an edge connecting two nodes. The result is an undirected graph in which the spatial relationships between the NPs are mapped directly into a network of nodes and edges.

To create this graph, we first assigned a node to every NP segmented in each of the TEM movie frames. For each NP, we evaluated the center-to-center distance with every other NP in the system. If the distance between two NPs was less than the defined threshold *rc*, then an unweighted edge was drawn between the corresponding nodes in the graph. We used distance thresholding because it captures the strongest nearest-neighbor interactions and is generalizable, requiring only tracked NP positions as inputs. The process was repeated for all particle pairs in the system, ensuring that all nearest-neighbor connections were accurately captured in the graph.

We also considered alternative ways to connect edges, such as weighing the physical distance of NPs with different forms of interaction potentials. There are many possible choices for how to weight edges, but at least some choices do not significantly change our analysis.

Once all the edges were defined, the resulting graph provided a direct representation of the positional relationships among the NPs in the assembly, where the nodes and edges correspond to the particles and their spatial interactions, respectively.

Although this graph construction describes the primary "interaction graph" used for most of the analyses presented here, we also used an "auxiliary graph" for analysis of mesocrystal structures. In addition to the separation of two particles being below the 1.15× threshold, edges were only added in the auxiliary graph if the two particles also had orientations that were aligned within 10°, as shown in fig. S1B. Because the nanocubes considered here had fourfold symmetry in this 2D assembly, this orientation step normalized the directors of the particles to between 0° and 90° before checking the difference or alignment between those directors. Once the auxiliary graph was obtained, mesocrystals were defined as connected components in the auxiliary graph that had at least four particles.

Graph curvature

ORC: The ORC (*49*) is a concept derived from Riemannian geometry and adapted to discrete structures such as graphs and networks. In continuous manifolds, positive curvature characterizes spherical surfaces where geodesics converge, whereas the negative curvature describes hyperbolic surfaces with diverging geodesics (see Fig. 2A and fig. S3A for a schematic geometric representation). The zero curvature corresponds to Euclidean flat surfaces with parallel geodesics. The ORC provides a measure of the "bending" or "curvature" of the space in a manner similar to classical Ricci curvature but is specifically tailored to metric spaces and graphs. The ORC concept has found applications in various fields, including network analysis and biological and economic networks, due to its ability to capture intrinsic geometric properties of complex structures (*68*).

The ORC is defined using the notion of Wasershtein distance (*69*) (sometimes spelled as Vaserstein, with original spelling in Russian being Л. Н. Васерштейн, and also known as the Earth mover's distance or the Earthmover distance) between probability measures. For a given graph $G = (V, E)$ with vertex set V and edge set E, the ORC along an edge (u, v) is defined as

$$ORC(u,v) = 1 - \frac{W_1(m_u, m_v)}{d(u,v)}$$

where $W_1(m_u, m_v)$ is the Waserstein distance between the probability measures m_u and m_v centered at vertices u and v, respectively, and $d(u, v)$ is the graph distance between vertices u and v. The Wasserstein distance is given by

$$W_1(m_u, m_v) = \inf_{\mu_{u,v} \in \Pi(m_u, m_v)} \sum_{(u',v') \in V \times V} d(u', v') \mu_{u,v}(u', v')$$

with $\Pi(m_u, m_v)$ being the set of probability measures $\mu_{u,v}$ that satisfies

$$\sum_{v' \in V} \mu_{u,v}(u', v') = m_u(u'), \ \sum_{u' \in V} \mu_{u,v}(u', v') = m_v(v')$$

The ORC has proven to be a valuable tool in the areas of clustering and community detection within networks (*49*, *70*, *71*). By leveraging the curvature values, one can identify clusters or communities that exhibit strong intracluster and weak intercluster connectivity. In practical terms, edges with high positive curvature often indicate robust connections within the same community, whereas edges with negative curvature signify bridges between different communities. Edges with zero curvature resemble grid-like structures. This makes ORC particularly effective in detecting the modular structure of complex networks, aiding in the identification of natural groupings within the network.

FRC and AFRC: The FRC (*72*) is a concept in discrete differential geometry that extends the notion of Ricci curvature from smooth Riemannian manifolds to combinatorial and discrete structures such as graphs and simplicial complexes. This curvature provides a measure of the "bending" of the space in a manner that is computationally efficient and suitable for combinatorial structures. For a given graph $G = (N, E)$ with set of nodes N interconnected by a set of edges E, the FRC of an edge $e = (u, v)$ between nodes u and v is defined based on the weights assigned to neighboring vertices and edges. Let w_u, w_v be the weights of the vertices u and v, respectively, and w_e be the weight of the edge e. Then, the FRC of an edge $e = (u, v)$ is given by

$$FRC(e) = w_e \left(\frac{w_u}{w_e} + \frac{w_v}{w_e} - \sum_{uvn} \left(\frac{\sqrt{w_u w_w}}{w_e} + \frac{\sqrt{w_v w_w}}{w_e} \right) \right)$$

where the summation P_{uvw} is taken over all nodes n that are adjacent to either nodes u or v. For graphs where all nodes and edges are unweighted or equal to 1, this simplifies to

$$FRC(e) = 4 - k(u) - k(v)$$

where $k(u)$ and $k(v)$ are the degree of each node defining the edge e.

In turn, we define AFRC (*73*) of an edge as

$$AFRC(e) = FRC(e) + 3m(e)$$

where m is the number of 3-cycles (triangles) of which e is a part. For graphs resulting from the reconfigurations of particles in 2D and with edges that cannot cross over one another, $m(e)$ can have a value of 0, 1, or 2.

Note that the FRC primarily focuses on local geometric properties and the AFRC accounts for multiparticle structures that are also known as simplicial complexes. The latter are particularly important in capturing polyadic interactions, which refer to interactions involving more than two elements simultaneously. Traditional graph-based models focus on pairwise relationships (edges), and simplicial complexes extend this to higher-dimensional structures [e.g., vertices correspond to individual entities such as nodes in a graph, edges (1-simplices) represent pairwise interactions, and triangles (2-simplices) capture interactions between three entities at once]. Also note that AFRC provides a computationally efficient way to explore the geometric and topological properties of complex weighted networks. This has been used in various applications, including brain networks and phase transition analysis (*74*).

Electromagnetic simulations for gold NP assemblies

Electromagnetic simulations were conducted at 14 designated time points throughout the entire self-assembly process of gold NPs. Using LPTEM images, we determined the geometric factors of the gold NPs and performed 3D modeling using Autodesk's 3ds Max (Autodesk, Inc., USA) software. Additionally, based on the LPTEM images and particle-tracking information (including coordinate and rotational data), we accurately replicated the positions, orientations, and self-assembled structures of the gold NPs across the 14 time points. Subsequently, using the commercial software package Lumerical FDTD Solutions 2024R1.4 (Ansys, Inc., Canada), we computed the electromagnetic (optical) responses at each time point. The gold NPs were positioned in the x-y plane, and unpolarized light ranging from 300 to 900 nm was irradiated from the z-axis direction. We obtained data on light extinction, particularly scattering and backscattering, based on the positions and formed structures of time points. To minimize the effects of reflections at various boundaries, perfectly matched layer boundary conditions were applied. Additionally, the refractive index was determined based on the standard refractive index for the PBS solution in which the gold NPs were dispersed. Frequency-domain field and power monitors were placed to collect electric field distribution images at 820 nm. All simulations and calculations at each time point were conducted under the same conditions and factors.

kMC simulations for ITO assemblies

We performed kMC simulations of $N = 10{,}000$ nanocrystals of core radius $a = 6$ nm in a cubic periodic box of volume V at a core volume fraction $\eta = 4\pi a^3 N/(3V) = 0.01$ using customized software. Details were as reported previously (*65*). Particles interacted with the combination of a hardcore interaction and a square well attraction potential as follows

$$U(r) = \begin{cases} \infty, & r < \sigma_{HS} \\ \epsilon, & \sigma_{HS} < r < \sigma_{HS} + \delta \\ 0, & 0,\ r > \sigma_{HS} + \delta \end{cases}$$

where $\sigma_{HS} = 14.4$ nm is the thermodynamic diameter of the nanoparticles, ϵ refers to the depth of the square well potential, and $\delta = 0.05\sigma_{HS}$ is the width of the square well potential.

Optical properties calculation for ITO assemblies

The mutual polarization method was used to compute the optical properties of large-scale ITO NP assemblies in 3D. This method is an

efficient coupled-dipole method that uses matrix-free, spectrally accurate Ewald summation to solve the following linear equations for the coupled dipoles of the nanocrystals (*29*):

$$\mathbf{E}_0 = \sum_j \mathbf{M}_{ij}\mathbf{p}_j, \mathbf{M}_{ij} = \begin{cases} \frac{\mathbf{I}}{\alpha}, & i=j \\ \frac{\mathbf{I}-3\hat{r}_{ij}\hat{r}_{ij}}{4\pi r_{ij}^3}, & i\neq j \end{cases}$$

where $\mathbf{E}_0$ is the incident optical field, $\mathbf{p}_j$ is the dipole moment of particle j, $\alpha = 4\pi a^3(\varepsilon_p - \varepsilon_m)/(\varepsilon_p + 2\varepsilon_m)$ is the nanocrystal's dipole polarizability, ε_p is the particle permittivity, ε_m is the medium permittivity, a is the radius of the optical core, $\mathbf{r}_{ij} = \mathbf{x}_i - \mathbf{x}_j$, $\mathbf{x}_i$ is particle i's position, $r_{ij} = |\mathbf{r}_{ij}|$, and $\hat{\mathbf{r}}_{ij} = \mathbf{r}_{ij}$. The parameters for the particle permittivity ε_p and medium permittivity ε_m were reported in (*65*). The particle permittivity, ε_p, was derived from the experimental extinction spectrum of a nanocrystal dispersion fitted using the heterogeneous ensemble Drude approximation (HEDA) model (*75*).

The per-particle extinction cross sections of clustered particles were computed from the dipole moments by $C_{ext} = k\mathrm{Im}(\sum_{i=1}^{N_c} \mathbf{E}_0^* \bullet \mathbf{p}_i) / \left(N_c |\mathbf{E}_0|^2\right)$ (*29*), where k is the wavenumber of the incident optical field, N_c is the number of clustered particles, and Im(•) denotes the imaginary part. The extinction efficiency was defined as the ratio of the extinction cross section per particle to the geometrical area of a spherical nanoparticle, $Q_{ext} = C_{ext}/(\pi a^2)$. For comparison of extinction to the ORC, which is a property of graph edges and is independent of isolated particles, only clustered particles were included. Figure 5, F and H, shows extinction efficiency maxima as a function of simulation time. The trajectories of the fractions of clustered particles for the two systems are shown in fig. S19.

REFERENCES AND NOTES

1. E. Nakouzi *et al.*, Impact of solution chemistry and particle anisotropy on the collective dynamics of oriented aggregation. *ACS Nano* **12**, 10114–10122 (2018). doi: 10.1021/acsnano.8b04909; pmid: 30180540
2. C. A. Silvera Batista, R. G. Larson, N. A. Kotov, Nonadditivity of nanoparticle interactions. *Science* **350**, 1242477 (2015). doi: 10.1126/science.1242477; pmid: 26450215
3. C. Liu *et al.*, "Colloid–atom duality" in the assembly dynamics of concave gold nanoarrows. *J. Am. Chem. Soc.* **142**, 11669–11673 (2020). doi: 10.1021/jacs.0c04444; pmid: 32543864
4. Z. Ou, Z. Wang, B. Luo, E. Luijten, Q. Chen, Kinetic pathways of crystallization at the nanoscale. *Nat. Mater.* **19**, 450–455 (2020). doi: 10.1038/s41563-019-0514-1; pmid: 31659295
5. Z. Tang, N. A. Kotov, M. Giersig, Spontaneous organization of single CdTe nanoparticles into luminescent nanowires. *Science* **297**, 237–240 (2002). doi: 10.1126/science.1072086; pmid: 12114622
6. U. Gasser, E. R. Weeks, A. Schofield, P. N. Pusey, D. A. Weitz, Real-space imaging of nucleation and growth in colloidal crystallization. *Science* **292**, 258–262 (2001). doi: 10.1126/science.1058457; pmid: 11303095
7. B. Luo *et al.*, Hierarchical self-assembly of 3D lattices from polydisperse anisometric colloids. *Nat. Commun.* **10**, 1815 (2019). doi: 10.1038/s41467-019-09787-6; pmid: 31000717
8. Q. Chen, S. C. Bae, S. Granick, Directed self-assembly of a colloidal kagome lattice. *Nature* **469**, 381–384 (2011). doi: 10.1038/nature09713; pmid: 21248847
9. J. Kim *et al.*, Reconfigurable polymer shells on shape-anisotropic gold nanoparticle cores. *Macromol. Rapid Commun.* **39**, e1800101 (2018). doi: 10.1002/marc.201800101; pmid: 29722094
10. Y. Zhou, S. L. Bore, A. R. Tao, F. Paesani, G. Arya, Many-body potential for simulating the self-assembly of polymer-grafted nanoparticles in a polymer matrix. *NPJ Comput. Mater.* **9**, 224 (2023). doi: 10.1038/s41524-023-01166-6
11. Z. Shen *et al.*, Resolving nonequilibrium shape variations among millions of gold nanoparticles. *ACS Nano* **18**, 15576–15589 (2024). doi: 10.1021/acsnano.4c00378; pmid: 38810115
12. S.-H. Shin *et al.*, Direct observation of kinetic traps associated with structural transformations leading to multiple pathways of S-layer assembly. *Proc. Natl. Acad. Sci. U.S.A.* **109**, 12968–12973 (2012). doi: 10.1073/pnas.1201504109; pmid: 22822216
13. Y. Yan, J. Huang, B. Z. Tang, Kinetic trapping - a strategy for directing the self-assembly of unique functional nanostructures. *Chem. Commun.* **52**, 11870–11884 (2016). doi: 10.1039/C6CC03620A; pmid: 27494003
14. W. Jiang *et al.*, Emergence of complexity in hierarchically organized chiral particles. *Science* **368**, 642–648 (2020). doi: 10.1126/science.aaz7949; pmid: 32273399
15. A. Haji-Akbari, M. Engel, S. C. Glotzer, Phase diagram of hard tetrahedra. *J. Chem. Phys.* **135**, 194101 (2011). doi: 10.1063/1.3651370; pmid: 22112060
16. M. Uchimali, B. C. Rao, S. Vedantam, Constitutively informed multi-body interactions for lattice particle models. *Comput. Methods Appl. Mech. Eng.* **366**, 113052 (2020). doi: 10.1016/j.cma.2020.113052
17. B. Luo *et al.*, Unravelling crystal growth of nanoparticles. *Nat. Nanotechnol.* **18**, 589–595 (2023). doi: 10.1038/s41565-023-01355-w; pmid: 36997752
18. C. K. Ofosu *et al.*, Assessing depletion attractions between colloidal nanocrystals. *Sci. Adv.* **11**, eadv2216 (2025). doi: 10.1126/sciadv.adv2216; pmid: 40203119
19. A. Kim *et al.*, Patchy nanoparticles by atomic stencilling. *Nature* **646**, 592–600 (2025). doi: 10.1038/s41586-025-09605-8; pmid: 41094247
20. A. Kim *et al.*, Symmetry-breaking in patch formation on triangular gold nanoparticles by asymmetric polymer grafting. *Nat. Commun.* **13**, 6774 (2022). doi: 10.1038/s41467-022-34246-0; pmid: 36351911
21. A. Al Harraq, A. A. Hymel, E. Lin, T. M. Truskett, B. Bharti, Dual nature of magnetic nanoparticle dispersions enables control over short-range attraction and long-range repulsion interactions. *Commun. Chem.* **5**, 72 (2022). doi: 10.1038/s42004-022-00687-3; pmid: 36697688
22. S. C. Endres, L. C. Ciacchi, L. Mädler, A review of contact force models between nanoparticles in agglomerates, aggregates, and films. *J. Aerosol Sci.* **153**, 105719 (2021). doi: 10.1016/j.jaerosci.2020.105719
23. G. Zhu *et al.*, Self-similar mesocrystals form via interface-driven nucleation and assembly. *Nature* **590**, 416–422 (2021). doi: 10.1038/s41586-021-03300-0; pmid: 33597761
24. A. Kim *et al.*, Direct imaging of "patch-clasping" and relaxation in robust and flexible nanoparticle assemblies. *ACS Nano* **18**, 939–950 (2024). doi: 10.1021/acsnano.3c09710; pmid: 38146750
25. C. Qian *et al.*, Nanoscale phonon dynamics in self-assembled nanoparticle lattices. *Nat. Mater.* **24**, 1616–1625 (2025). doi: 10.1038/s41563-025-02253-3; pmid: 40528099
26. S. Lee, E. G. Teich, M. Engel, S. C. Glotzer, Entropic colloidal crystallization pathways via fluid-fluid transitions and multidimensional prenucleation motifs. *Proc. Natl. Acad. Sci. U.S.A.* **116**, 14843–14851 (2019). doi: 10.1073/pnas.1905929116; pmid: 31285316
27. I. U. Arachchige, S. L. Brock, Sol-gel methods for the assembly of metal chalcogenide quantum dots. *Acc. Chem. Res.* **40**, 801–809 (2007). doi: 10.1021/ar600028s; pmid: 17441681
28. D. A. Vecchio *et al.*, Spanning network gels from nanoparticles and graph theoretical analysis of their structure and properties. *Adv. Mater.* **34**, e2201313 (2022). doi: 10.1002/adma.202201313; pmid: 35403264
29. Z. M. Sherman *et al.*, Plasmonic response of complex nanoparticle assemblies. *Nano Lett.* **23**, 3030–3037 (2023). doi: 10.1021/acs.nanolett.3c00429; pmid: 36989531
30. X. Geng *et al.*, Atomically dispersed Pb ionic sites in PbCdSe quantum dot gels enhance room-temperature NO_2 sensing. *Nat. Commun.* **12**, 4895 (2021). doi: 10.1038/s41467-021-25192-4; pmid: 34385446
31. D. Z. Rocklin, S. Zhou, K. Sun, X. Mao, Transformable topological mechanical metamaterials. *Nat. Commun.* **8**, 14201 (2017). doi: 10.1038/ncomms14201; pmid: 28112155
32. W. Chen *et al.*, Formation and impact of nanoscopic oriented phase domains in electrochemical crystalline electrodes. *Nat. Mater.* **22**, 92–99 (2023). doi: 10.1038/s41563-022-01381-4; pmid: 36280702
33. P. Erdos, A. Renyi, On random graphs I. *Publ. Math.* **6**, 18 (1959).
34. D. J. Watts, S. H. Strogatz, Collective dynamics of 'small-world' networks. *Nature* **393**, 440–442 (1998). doi: 10.1038/30918; pmid: 9623998
35. Z. Ou, L. Yao, H. An, B. Shen, Q. Chen, Imaging how thermal capillary waves and anisotropic interfacial stiffness shape nanoparticle supracrystals. *Nat. Commun.* **11**, 4555 (2020). doi: 10.1038/s41467-020-18363-2; pmid: 32917872
36. L. Yao, Z. Ou, B. Luo, C. Xu, Q. Chen, Machine learning to reveal nanoparticle dynamics from liquid-phase TEM videos. *ACS Cent. Sci.* **6**, 1421–1430 (2020). doi: 10.1021/acscentsci.0c00430; pmid: 32875083
37. R. Albert, A.-L. Barabási, Statistical mechanics of complex networks. *Rev. Mod. Phys.* **74**, 47–97 (2002). doi: 10.1103/RevModPhys.74.47
38. A.-L. Barabási, M. Pósfai, *Network Science* (Cambridge Univ. Press, 2016).
39. S. M. Oh, Y. Lee, B. Kahng, Emergent properties in social networks with higher-order interactions. *Chaos Solitons Fractals* **199**, 116649 (2025). doi: 10.1016/j.chaos.2025.116649
40. M. J. Keeling, K. T. D. Eames, Networks and epidemic models. *J. R. Soc. Interface* **2**, 295–307 (2005). doi: 10.1098/rsif.2005.0051; pmid: 16849187
41. D. S. Bassett, E. T. Owens, K. E. Daniels, M. A. Porter, Influence of network topology on sound propagation in granular materials. *Phys. Rev. E Stat. Nonlin. Soft Matter Phys.* **86**, 041306 (2012). doi: 10.1103/PhysRevE.86.041306; pmid: 23214579
42. H. Zhang *et al.*, Graph theoretical design of biomimetic aramid nanofiber composites as insulation coatings for implantable bioelectronics. *MRS Bull.* **46**, 576–587 (2021). doi: 10.1557/s43577-021-00071-x
43. R. Simoes, J. Silva, A. Cadilhe, R. Vaia, Applications of the graph theory to the prediction of electrical and dielectric properties of nano-filled polymers. *Compos. Interfaces* **17**, 407–422 (2010). doi: 10.1163/092764410X513431

44. T. Yoshimura *et al.*, Exploring the full catalytic cycle of rhodium(i)-BINAP-catalysed isomerisation of allylic amines: A graph theory approach for path optimisation. *Chem. Sci.* **8**, 4475–4488 (2017). doi: 10.1039/C7SC00401J; pmid: 28970877
45. M. Aldeghi, C. W. Coley, A graph representation of molecular ensembles for polymer property prediction. *Chem. Sci.* **13**, 10486–10498 (2022). doi: 10.1039/D2SC02839E; pmid: 36277616
46. F. C. Kalutantirige *et al.*, Beyond nothingness in the formation and functional relevance of voids in polymer films. *Nat. Commun.* **15**, 2852 (2024). doi: 10.1038/s41467-024-46584-2; pmid: 38605028
47. D. A. Vecchio, S. H. Mahler, M. D. Hammig, N. A. Kotov, Structural analysis of nanoscale network materials using graph theory. *ACS Nano* **15**, 12847–12859 (2021). doi: 10.1021/acsnano.1c04711; pmid: 34313122
48. R. Yang *et al.*, Graph theoretical description of phase transitions in complex multiscale phases with supramolecular assemblies. *Adv. Sci. (Weinh.)* **11**, e2402464 (2024). doi: 10.1002/advs.202402464; pmid: 38952077
49. J. Sia, E. Jonckheere, P. Bogdan, Ollivier-Ricci curvature-based method to community detection in complex networks. *Sci. Rep.* **9**, 9800 (2019). doi: 10.1038/s41598-019-46079-x; pmid: 31278341
50. R. Forman, Bochner's method for cell complexes and combinatorial Ricci curvature. *Discrete Comput. Geom.* **29**, 323–374 (2003). doi: 10.1007/s00454-002-0743-x
51. V. Kuznetsova *et al.*, Graph–property relationships for complex chiral nanodendrimers. *ACS Nano* **19**, 6095–6106 (2025). doi: 10.1021/acsnano.4c12964; pmid: 39903700
52. E. Ndong Mintsa, P. Germain, S. Amokrane, Bond lifetime and diffusion coefficient in colloids with short-range interactions. *Eur. Phys. J. E Soft Matter* **38**, 21 (2015). doi: 10.1140/epje/i2015-15021-8; pmid: 25813606
53. B. Lu *et al.*, Tunable subnanometer gaps in self-assembled monolayer gold nanoparticle superlattices enabling strong plasmonic field confinement. *ACS Nano* **17**, 12774–12787 (2023). doi: 10.1021/acsnano.3c03804; pmid: 37354449
54. P. S. S. dos Santos, J. M. M. M. de Almeida, I. Pastoriza-Santos, L. C. C. Coelho, Advances in plasmonic sensing at the NIR—A Review. *Sensors* **21**, 2111 (2021). doi: 10.3390/s21062111; pmid: 33802958
55. S. Link, M. A. El-Sayed, Size and temperature dependence of the plasmon absorption of colloidal gold nanoparticles. *J. Phys. Chem. B* **103**, 4212–4217 (1999). doi: 10.1021/jp984796o
56. P. Nordlander, C. Oubre, E. Prodan, K. Li, M. I. Stockman, Plasmon hybridization in nanoparticle dimers. *Nano Lett.* **4**, 899–903 (2004). doi: 10.1021/nl049681c
57. S.-E. Kim *et al.*, Near-infrared plasmonic assemblies of gold nanoparticles with multimodal function for targeted cancer theragnosis. *Sci. Rep.* **7**, 17327 (2017). doi: 10.1038/s41598-017-17714-2; pmid: 29229979
58. M. Randić, Graph theoretical descriptors of two-dimensional chirality with possible extension to three-dimensional chirality. *J. Chem. Inf. Comput. Sci.* **41**, 639–649 (2001). doi: 10.1021/ci000115m; pmid: 11410041
59. X. Mao, N. Kotov, Complexity, disorder, and functionality of nanoscale materials. *MRS Bull.* **49**, 352–364 (2024). doi: 10.1557/s43577-024-00698-6
60. M. Gell-Mann, What is complexity? *Complexity* **1**, 1–5 (1995).
61. Ali Bilal Cambel, *Applied Chaos Theory - A Paradigm for Complexity* (Academic Press, 1992).
62. P. Grassberger, Toward a quantitative theory of self-generated complexity. *Int. J. Theor. Phys.* **25**, 907–938 (1986). doi: 10.1007/BF00668821
63. B. A. Huberman, T. Hogg, Complexity and adaptation. *Physica D* **22**, 376–384 (1986). doi: 10.1016/0167-2789(86)90308-1
64. R. López-Ruiz, H. L. Mancini, X. Calbet, A statistical measure of complexity. *Phys. Lett. A* **209**, 321–326 (1995). doi: 10.1016/0375-9601(95)00867-5
65. J. Kang *et al.*, Colloidal phase control in plasmonic metal oxide nanocrystals via competitive metal–ligand equilibria. *Angew. Chem. Int. Ed.* **64**, e18965 (2025). doi: 10.1002/anie.202518965; pmid: 41186098
66. M. N. O'Brien, M. R. Jones, K. A. Brown, C. A. Mirkin, Universal noble metal nanoparticle seeds realized through iterative reductive growth and oxidative dissolution reactions. *J. Am. Chem. Soc.* **136**, 7603–7606 (2014). doi: 10.1021/ja503509k; pmid: 24830921
67. J. A. Anderson, J. Glaser, S. C. Glotzer, HOOMD-blue: A Python package for high-performance molecular dynamics and hard particle Monte Carlo simulations. *Comput. Mater. Sci.* **173**, 109363 (2020). doi: 10.1016/j.commatsci.2019.109363
68. R. S. Sandhu, T. T. Georgiou, A. R. Tannenbaum, Ricci curvature: An economic indicator for market fragility and systemic risk. *Sci. Adv.* **2**, e1501495 (2016). doi: 10.1126/sciadv.1501495; pmid: 27386522
69. L. N. Vaserstein, Markov processes over denumerable products of spaces, describing large systems of automata. *Probl. Pereda. Inf.* **5**, 64–72 (1969).
70. D. Leite, D. Baptista, A. A. Ibrahim, E. Facca, C. De Bacco, Community detection in networks by dynamical optimal transport formulation. *Sci. Rep.* **12**, 16811 (2022). doi: 10.1038/s41598-022-20986-y; pmid: 36207412
71. J. Sia, W. Zhang, E. Jonckheere, D. Cook, P. Bogdan, Inferring functional communities from partially observed biological networks exploiting geometric topology and side information. *Sci. Rep.* **12**, 10883 (2022). doi: 10.1038/s41598-022-14631-x; pmid: 35760826
72. M. Weber, J. Jost, E. Saucan, Forman-Ricci flow for change detection in large dynamic data sets. *Axioms* **5**, 26 (2016). doi: 10.3390/axioms5040026
73. L. Fesser, S. Serrano de Haro Iváñez, K. Devriendt, M. Weber, R. Lambiotte, Augmentations of Forman's Ricci curvature and their applications in community detection. *J. Phys. Complex.* **5**, 035010 (2024). doi: 10.1088/2632-072X/ad64a3
74. M. R. Znaidi *et al.*, A unified approach of detecting phase transition in time-varying complex networks. *Sci. Rep.* **13**, 17948 (2023). doi: 10.1038/s41598-023-44791-3; pmid: 37864007
75. S. L. Gibbs *et al.*, Intrinsic optical and electronic properties from quantitative analysis of plasmonic semiconductor nanocrystal ensemble optical extinction. *J. Phys. Chem. C Nanomater. Interfaces* **124**, 24351–24360 (2020). doi: 10.1021/acs.jpcc.0c08195
76. D. Frenkel, B. Smit, *Understanding Molecular Simulation: From Algorithms to Applications* (Elsevier, 2001).

ACKNOWLEDGMENTS

Funding: This work was supported by the Center for Complex Particle Systems (COMPASS) Science and Technology Center (J.H., P.P., J.S., S.B., C.Q., S.L., L.Y., Q.C., X.M., P.B., and N.A.K.); the US National Science Foundation (NSF cooperative agreement 2243104, career award CPS-1453860, grant MCB-1936775, and grant CNS-1932620 to J.S. and P.B. and DMREF project CBET-2323482 to T.M.T., D.J.M., and D.Q.); the US Army Research Office (ARO grant W911NF-23-1-0111 to J.S. and P.B.); NSF under the); Defense Advanced Research Projects Agency (DARPA Young Faculty Award to J.S. and P.B. and DARPA Director Fellowship Award under grant N66001-17-1-4044 to J.S. and P.B.); the National Institutes of Health (NIH grants R01 AG 079957 and RF1 AG 082201 to J.S. and P.B.); the Office of Naval Research (MURI grant N00014-20-1-2479 to J.H., X.M., Q.C., and N.A.K.); and the Welch Foundation (grant F-1696 to T.M.T., D.J.M., and D.Q.). **Author contributions:** Analysis of LPTEM movies: P.P., C.Q., L.Y., Q.C.; Calculation of optical properties: S.B., D.Q., T.M.T., D.J.M., N.A.K.; Conceptualization: N.A.K.; Establishment of the graph analysis workflow: J.S., P.B.; LPTEM experiments: C.Q., S.L.; Manuscript drafting: J.H., P.P.; Self-assembly simulations and simulation analysis: J.H., D.Q., T.M.T., D.J.M., X.M.; Supervision of the work: N.A.K., Q.C., X.M., P.B., T.M.T., D.J.M.. All authors contributed to the editing and revision of the manuscript **Competing interests:** The authors declare no competing interests. **Data, code, and materials availability:** All data are available in the main text or the supplementary materials. Raw data are available online to any researcher for purposes of reproducing or extending the analysis. No materials transfer agreements are required. All related code is available on GitHub at https://github.com/jhallstrom-umich/graph-curvature-paper.

SUPPLEMENTARY MATERIALS

science.org/doi/10.1126/science.aeb5134
Supplementary Text; Figs. S1 to S19; Tables S1 to S2; References; Movies S1 to S4

Submitted 17 August 2025; accepted 17 February 2026

10.1126/science.aeb5134

Decoding collective dynamics and complexity in nanoparticle assemblies using graph theory

Jonas Hallstrom, Puquan Pan, Jayson Sia, Sangwok Bae, Dingwen Qian, Chang Qian, Sindy Liu, Lehan Yao, Thomas M. Truskett, Delia J. Milliron, Qian Chen, Xiaoming Mao, Paul Bogdan, and Nicholas A. Kotov

Science **392** (6799), eaeb5134. DOI: 10.1126/science.aeb5134

Editor's summary

Self-assembly of nanoparticles often produces structures that lie between crystalline order and complete disorder, but describing these states remains challenging. Hallstrom *et al*. applied graph theory to quantify the evolution of truncated gold nanocube assemblies imaged using electron microscopy. They showed that Ollivier-Ricci curvature and augmented Forman-Ricci curvature can track global structural complexity and local energetic stability, respectively. Moreover, they revealed that an intermediate, partially ordered network coincides with the strongest plasmonic responses. Finally, they confirmed that this theory is generalizable to other systems such as gold nanoprisms and indium tin oxide nanospheres. —Jack Huang